buildings

MDPI

Article

The Composition and Performance of Iron Ore Tailings in Steel Slag-Based Autoclaved Aerated Concrete

Hao Zhou [1], Yang Jiang [2], Jiaqing Wang [3], Houhu Zhang [1], Binbin Qian [4], Bing Ma [1,*] and Yueyang Hu [5,*]

[1] Nanjing Institute of Environmental Sciences, Ministry of Ecology and Environment of the People's Republic of China, Nanjing 210042, China
[2] Advanced Green-Materials, Institute of China Energy Engineering Corporation, Beijing 100022, China
[3] College of Civil Engineering, Nanjing Forestry University, Nanjing 210037, China
[4] School of Chemistry and Environmental Engineering, Yancheng Teachers University, Yancheng 224002, China
[5] College of Materials Science and Engineering, Yancheng Institute of Technology, Yancheng 224000, China
* Correspondence: mabing@nies.org (B.M.); huyueyang1989@ycit.edu.cn (Y.H.)

Abstract: Iron ore tailings (IOTs) are byproducts of the iron mining industry that have gained significant attention in recent years due to their potential for comprehensive utilization. This study investigates how blending steel slag with IOTs (a siliceous raw material) instead of lime (a calcareous raw material) affects slurry foaming properties, mechanical properties, and reaction mechanisms of autoclaved aerated concrete (AAC). The results indicate that the sample containing 24% IOT content exhibited the best performance, with a bulk density of 640 kg/m^3 and a compressive strength of 4.1 MPa. In addition, IOTs not only served as a filling material but also acted as a carrier for the growth of tobermorite. Tobermorite was combined with the unreacted iron tailing and its neighboring tobermorite to form a cohesive whole. This study provides valuable insights into the potential for IOTs to improve the properties of AAC when used as a supplementary material. The findings also suggest that the comprehensive utilization of IOTs and other industrial byproducts have the potential to contribute to the development of sustainable building materials and reduce the environmental impact of the mining industry.

Keywords: iron ore tailings; steel slag; autoclaved aerated concrete; tobermorite

Citation: Zhou, H.; Jiang, Y.; Wang, J.; Zhang, H.; Qian, B.; Ma, B.; Hu, Y. The Composition and Performance of Iron Ore Tailings in Steel Slag-Based Autoclaved Aerated Concrete. *Buildings* **2023**, *13*, 2942. https://doi.org/10.3390/buildings13122942

Academic Editor: Binsheng (Ben) Zhang

Received: 10 October 2023
Revised: 12 November 2023
Accepted: 20 November 2023
Published: 25 November 2023

1. Introduction

Autoclaved aerated concrete (AAC), a lightweight building material, is widely used in buildings due to its good insulation properties, high heat resistance, low density, low shrinkage, and sufficient strength [1,2]. The densities of the final AAC products are generally between 400 and 800 kg/m^3, and the compressive strengths of the AAC range from 1.5 to 7.5 MPa [3]. Generally, there are two main types of traditional commercial AAC: ash-based and sand-based AAC. The main raw material for the ash base is fly ash or some materials with relatively high pozzolanic activity. The main raw materials for the sand base are quartz sand, river sand, or siliceous materials with low activity. Currently, the limitation on CO_2 emissions has led to decreased production of cement in China, which has increased the price of supplementary cementitious materials. The prices of raw materials used in AAC have increased sharply. Therefore, the utilization of silica-based solid waste as a substitute material for fly ash in AAC has an important influence on the development of the AAC industry.

IOTs are solid mineral wastes with low useful metal content that are produced after iron ore has been crushed, screened, regraded, and treated by flotation [4]. In 2020, the total volume of tailings generated from solid waste in China was approximately 12.72 billion tons, with IOTs generating the largest volume at approximately 5.2 billion tons, accounting for 40.9% of the total generation of tailings. The large volume of generated IOTs has resulted in the occupation of large amounts of land and environmental damage [5–7].

The chemical composition of IOTs mainly depends on the mineralogy of iron ore. IOTs contain mainly SiO_2, Al_2O_3, Fe_2O_3, CaO, and small fractions of metal oxides (MgO, Na_2O, K_2O, TiO_2, and Mn_2O_3) [7]. During crushing and screening, IOTs can be divided into coarse tailings and fine tailings according to the granulometric classification. Most of the coarse tailings are made into manufactured sand. However, the presence of heavy metals such as Mn in the remaining fine tailings limits their application in the cement industry. Many studies have shown that increasing the fineness of IOTs can effectively promote their activity [5,8–10]. However, the production of ultrafine powder leads to a higher cost of energy, which increases the production cost of building materials. Therefore, the utilization of fine tailings without grinding in AAC has a significant influence on the AAC industry. However, because of the higher content of unreacted iron tailings in the AAC, the addition of fine tailings leads to a higher density.

Traditionally, Al powder is used in the AAC industry to decrease the density of AAC. However, the content of Al powder used in AAC has an optimization value, and the excess content of Al powder cannot improve the foaming. Currently, with their porous character, some silica-rich industrial waste catalysts are also utilized in the preparation of AAC. Zeolite Socony Mobil-Number 5 (ZSM-5) is widely used as a cracking catalyst in the petroleum refining industry and for the drying, purification, separation, and recovery of gases and liquids [11,12]. However, repeated use can cause the coke to block the pore channels, cover the active site, and eventually deactivate ZSM-5 [11,13]. The common way to dispose of deactivated ZSM-5 is by landfill disposal, which causes significant environmental stress [14]. Deactivated ZSM-5 contains a large amount of amorphous silica, and the air in its pores can be released at high temperatures [3,13,15]. Hence, deactivated ZSM-5 has potential applications in AAC and can be used as an auxiliary foaming material and is an excellent siliceous raw material.

The objective of this paper is to investigate the feasibility of IOTs in the preparation of AAC from steel slag as a calcareous raw material. The effect of iron ore tailing substitution and deactivated ZSM-5 as auxiliary foaming materials on the foaming properties is investigated. In addition, the mineral composition of AAC, the microstructure of minerals, and the porosity of AAC are studied in this investigation.

2. Materials and Methods

2.1. Materials

The raw materials adopted to fabricate AAC were iron ore tailing, steel slag, and deactivated ZSM-5. The IOTs were supplied by a local steelmaking plant in Jinan, Shandong Province, China. The steel slag was obtained from Lingshou Shihang Building Materials Co., Ltd., Shijiazhuang, Hebei, China. The deactivated ZSM-5 was produced by Zibo Hengyi Chemical Technology Co., Ltd., Zibo, Shandong Province, China. The cement, which is ordinary Type I Portland cement OPC (CEM I 42.5 N), came from Yancheng, China. Quicklime, with >98% effective calcium oxide content, was purchased from Yancheng, China. Gassing material aluminum powder was obtained from Yancheng, China. Gypsum (analytical grade, purity $\geq$ 99%) was supplied by Nanjing Chemical Reagent Co., Nanjing, Jiangsu Province, China. The particle size distributions of four dry powders (steel slag, deactivated ZSM-5, cement and IOTs) are shown in Figure 1. The chemical characteristic results of the raw materials are provided in Table 1. Figure 2 shows the X-ray diffraction (XRD) patterns of the raw materials (IOTs, steel slag and deactivated ZSM-5). The main sharp peaks in deactivated ZSM-5 indicate the existence of ZSM-5, accompanied by some mineral phases of quartz and cristobalite. Clearly, the major constituent crystalline phase quartz is observed in the IOTs pattern, along with some weak peaks such as hematite, magnetite, albite and microcline. Compared with the deactivated ZSM-5 and IOTs, the mineral phases in steel slag are relatively complex. Mineral phases include C_2F, $Ca(OH)_2$, C_3S, C_2S, RO, CaO, quartz, and kirschsteinite.

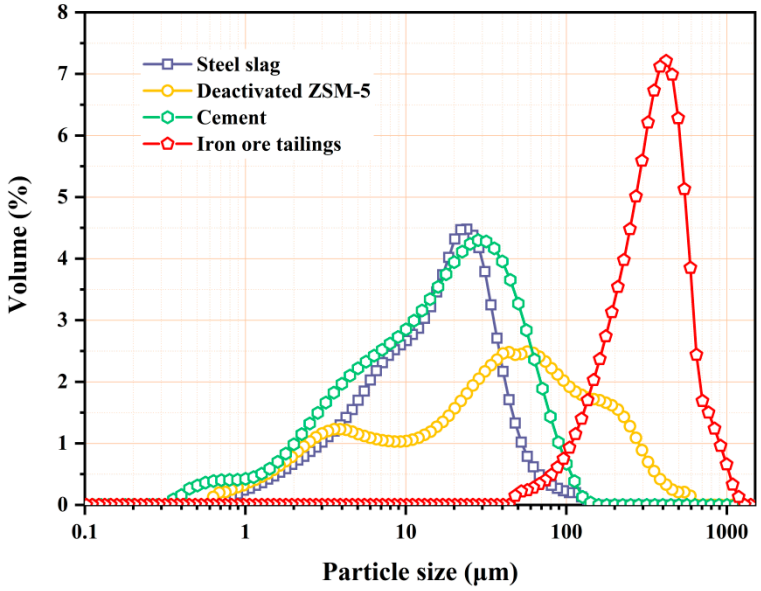

Figure 1. Particle size distributions of the raw materials.

Table 1. Chemical components of the raw materials (%).

Component	SiO_2	Al_2O_3	CaO	MgO	Fe_2O_3	SO_3	Na_2O	K_2O	TiO_2	Mn_2O_3	LOI
Iron ore tailings	76.83	11.12	0.84	0.36	2.89	-	2.33	4.99	0.26	0.03	0.35
Steel slag	20.23	4.54	61.45	2.74	3.05	2.56	0.51	0.70	-	-	4.22
Deactivated ZSM-5	93.89	0.53	0.18	1.52	0.24	-	-	-	-	-	3.64
CEM I 42.5N	22.26	5.89	60.17	2.35	2.96	2.49	0.29	0.71	-	-	2.88

2.2. Mix Proportions and Preparation

The specific mix designs of the individual samples are shown in Table 2. The setting of IOT content was based on the conventional calcium-to-silicon (Ca/Si) ratio (0.7–0.8) of sand-based AAC. The Ca/Si ratios of samples SIOT0-SIOT24 were 0.92–0.62, which are included in the sand-based AAC system. A single siliceous material does not provide enough silica for the hydrothermal synthesis reaction and therefore needs to be supplemented by the introduction of other high-silica materials. Deactivated ZSM-5 is an auxiliary foaming material, and its high silica content makes it a suitable option. In addition, the water-to-solid ratio (W/S) of individual samples was controlled at 0.78. In addition, 0.15% aluminum powder was introduced in the matrix materials.

Table 2. Detailed mix compositions of individual AAC samples (wt%).

Sample Number	Calcareous Raw Material		Siliceous Raw Material	IOT	Gypsum
	OPC	Steel Slag	Deactivated ZSM-5		
SIOT0	15	58	24	0	3
SIOT6	15	58	24	6	3
SIOT12	15	58	24	12	3
SIOT18	15	58	24	18	3
SIOT24	15	58	24	24	3

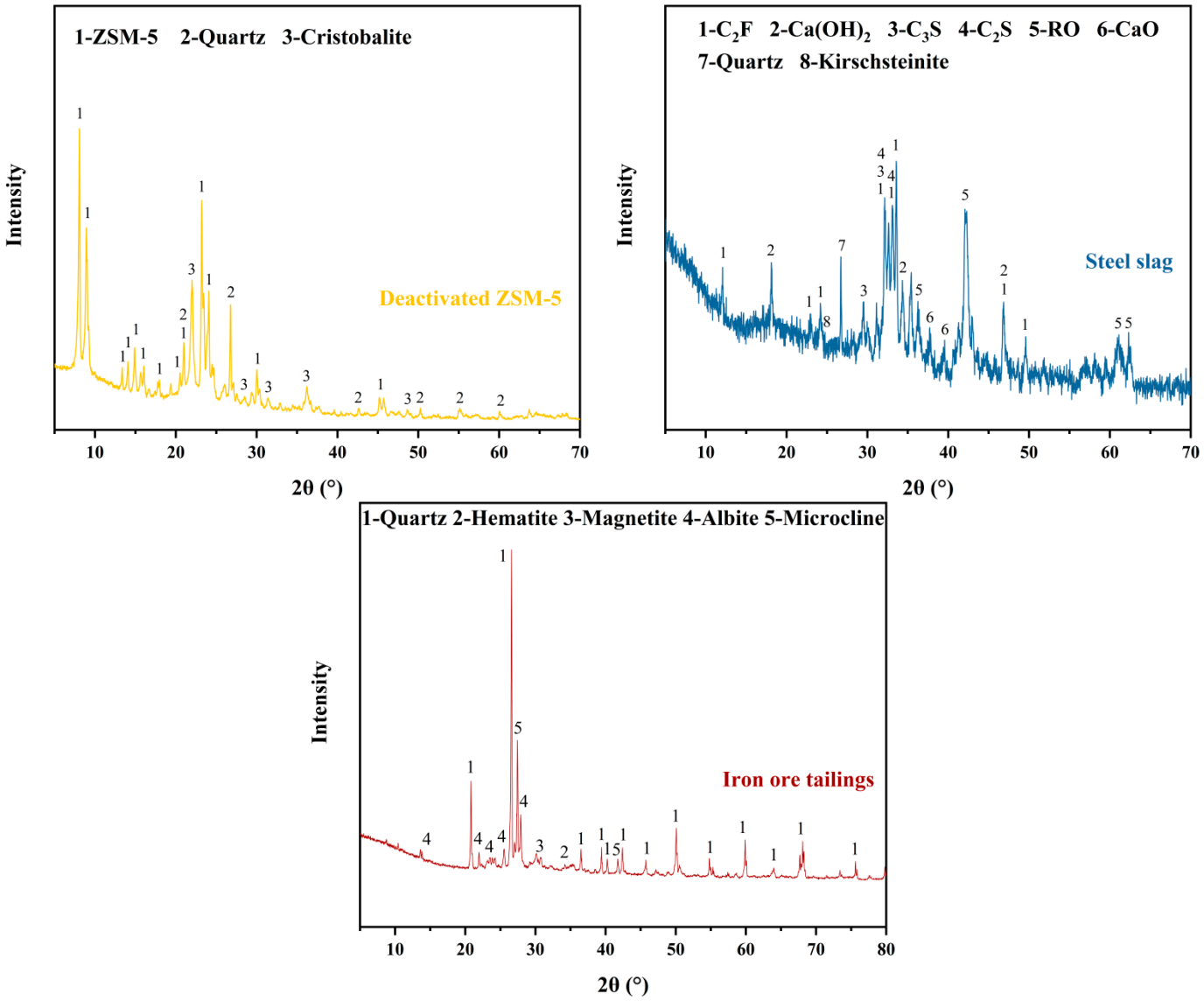

Figure 2. The XRD patterns of the raw materials.

First, the raw materials, including cement, steel slag, deactivated ZSM-5, IOTs, and gypsum, were weighed and premixed. Then, the premixing materials were poured into the mixing pot, followed by the intended amount of water and stirring for 4 min until a uniform mixture was achieved. Finally, aluminum powder was added to the mixing pot and stirred for 40 s. The fresh slurry was cast in a 100 mm × 100 mm × 100 mm mold and then put into a constant temperature curing box with a temperature of 65 °C for 12 h to achieve the adequate demolding strength. To ensure that the samples used in the mechanical tests are of the same shape, the expanded part outside the volume of the mold was removed with a saw, followed by numbering. The obtained samples were placed in an autoclave with the temperature and pressure set at 185 °C and 1.8 MPa, respectively.

2.3. Characterization

2.3.1. Raw Materials

The crystalline phases of the steel slag, deactivated ZSM-5, and IOT were identified using powder X-ray diffraction (XRD). A particle size analyzer was employed to analyze the particle size distributions of the raw materials.

2.3.2. Foaming Testing

The volume expansion of the slurry in the measuring cylinder was used to reflect the overall expansion effect. Part of the slurry (100 mL) was poured into a measuring cylinder with a maximum capacity of 250 mL, which was placed in a constant temperature oven at 65 °C. The expansion volume of the slurry in the cylinder was recorded every three minutes until the expansion value stabilized.

2.3.3. Fluidity of Slurry

A cement mortar fluidity tester (NLD-3) was adopted to measure the fluidity of the slurry in accordance with GB/T2419-2005 [16]. In this experiment, the shaking step was canceled because of the high fluidity of the slurry.

2.3.4. Compressive Strength and Bulk Density

The specimens were tested for bulk density and compressive strength in accordance with GB/T 11969-2008 [17]. Three AAC samples were prepared for each performance test to ensure repeatability, and the average of the three tests was taken for each case.

2.3.5. Reaction Product Analysis

All samples tested were selected from crushed samples at the end of the compression tests, and hydration was terminated using anhydrous ethanol prior to all testing. Samples for XRD, Fourier-transform infrared spectroscopy (FTIR), and thermogravimetry-differential thermal analysis (TG-DTA) were ground to a fine powder, and samples for scanning electron microscopy (SEM) and mercury intrusion porosimetry (MIP) tests were selected from small cubes of approximately 1 cm.

The DX-2700 (Fangyuan, Dandong, China) was used for the mineral phase analysis of the samples, using the Kα1 radiometric reflection of Cu with a range from 5–80° at a scan speed of 5°/min.

TG-DTA of the reaction products was carried out using an STA 449C3/G thermogravimeter (NETZSCH, Selbu, Germany). The sample powder was placed in a small alumina crucible and heated from 40 °C to 1100 °C at a flow rate of 40 μL/min at 10 °C/min in a nitrogen-protected atmosphere.

The chemical bonds formed in the reaction products were determined by FTIR using a NEXUS 670 spectrometer (Nicolet, Madison, WI, USA) in the wavenumber range of 400–4000 cm^{-1} with a resolution of 4 cm^{-1}.

The pore size distribution and porosity were measured using Auto Proe 9500 IV (Mack, Atlanta, GA, USA), with max. and min. pressures restricted to 0.6 psia and 33,000 psia, respectively.

The equipment used for microscopic analysis of the samples was a Nano SEM450 (FEI, Hillsboro, OR, USA) equipped with energy dispersive spectroscopy (EDS) analysis. All samples were gold plated prior to testing to improve conductivity.

3. Results and Discussion

3.1. Determination of Slurry pH

The alkaline environment of the slurry influences the foaming process of aluminum powder. In this study, IOTs were considered to be an acidic material due to the silica content of over 60% [18], which has a potentially detrimental effect on the alkaline environment of the slurry. It is therefore necessary to discuss the effect of IOT contents on the pH values of the slurry. The pH values of the slurry are shown in Figure 3. Clearly, the pH value decreases from 12.65 to 12.47 with the increasing IOT content. The pH values of the slurry were maintained within the appropriate range, although the increased IOT content reduced the pH value.

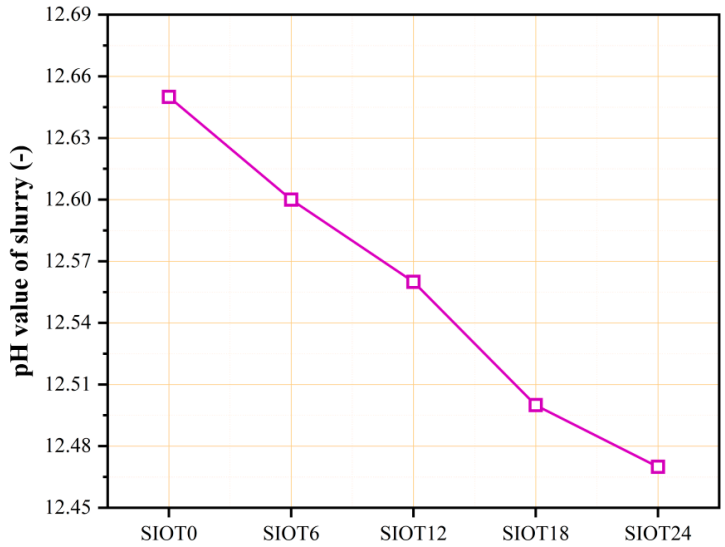

Figure 3. pH values of the slurry with different IOT contents.

3.2. Determination of Slurry Fluidity

The fluidity of the slurry is an important technological parameter affecting the quality of AAC. The large fluidity of aerated concrete slurry can cause gases to escape very quickly, so that the pore structure of the product can collapse during precuring. However, the gas does not escape in time when the fluidity of the slurry is low, resulting in horizontal fracture of the product. For this reason, it is necessary to study the effect of fluidity on aerated concrete.

Figure 4 displays the effect of the IOT content on the fluidity of the aerated concrete slurry. As shown in Figure 4, the fluidities of samples SIOT0, SIOT6, SIOT12, SIOT18, and SIOT24 were 191, 195, 209, 220, and 233 mm, respectively. It is clear that increasing the IOT content thereby changes the fluidity of the slurry. Compared to other raw materials, IOTs are coarser in particle size and have a smaller specific surface area. Less water is required to wrap the IOTs, and more free water is used for lubrication, thereby improving the fluidity of the slurry.

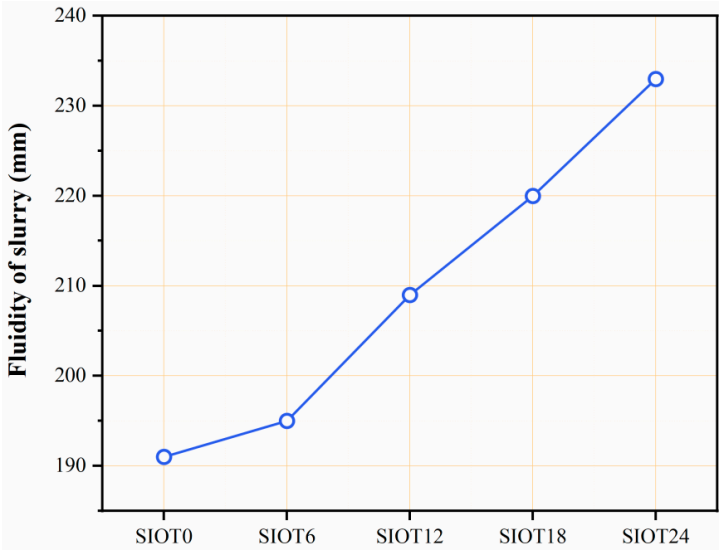

Figure 4. Slurry fluidity with different IOT contents.

3.3. Foaming Properties of The Slurry

The foaming properties of the slurry are an important process in the formation of the pore structure of AAC [5,19]. Aluminum powder is the most commonly used foaming agent in the production of AAC, and lime hydration provides the necessary alkaline environment for the foaming process [20]. However, the foaming process in this test had to consider the effects of two things: (1) the full replacement of lime by steel slag and (2) auxiliary foaming raw material—deactivated ZSM-5.

Figure 5 shows the effect of the IOT admixtures on the foaming effect and foaming time of aerated concrete. It is clear that the foaming process can be divided into two stages. In the first stage (<40 min), it can be seen that the slurry expands rapidly within the first forty minutes, with an expansion rate of 80%, and that the slurry with high IOT admixtures has a higher expansion rate than the slurry with low admixture. This is because the high fluidity of the slurry demonstrates less resistance to the rise of air bubbles in the slurry, which promotes early expansion. In the first stage, as the slurry temperature rises in the maintenance chamber, the release of gas from the pores of the deactivated ZSM-5 accompanied by the gassing of the aluminum powder is the main reason for the volume expansion of the slurry. In the second stage (>40 min), it can be seen that, after forty minutes, the expansion of the slurry slows down; the expansion accounts for approximately 20% of the final expansion value, and the increase in the iron tailing admixture has a minimal effect on the final expansion. In the second stage, the smooth gassing of the remaining aluminum powder is the main reason for the swelling of the slurry. In addition, the increase in IOT admixtures also significantly changes the foaming termination time of the slurry. This is mainly due to the high flowability of the slurry with high IOT doses, which prolongs the thickening time of the slurry. Therefore, the foaming termination time of the slurry increases with the increasing IOT dose. The final foaming end times vary between 69–90 min.

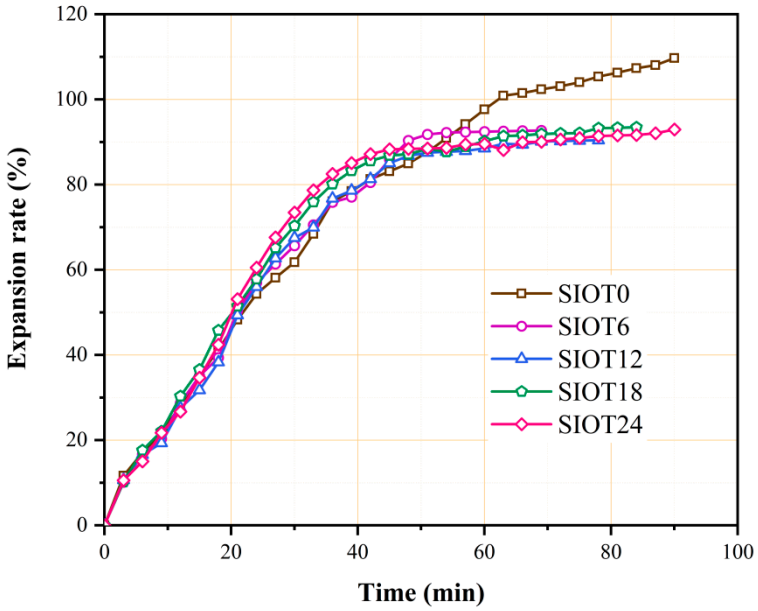

Figure 5. Expansion rates of the slurry with different IOT contents.

3.4. Compressive Strength and Bulk Density

Figure 6 shows the compressive strengths and bulk densities of the SIOT0, SIOT6, SIOT12, SIOT18, and SIOT24 samples. It is clear that the bulk density increases with the increasing IOT admixture. The foaming process is an important factor affecting bulk density. In Section 3.3, the increase in IOT admixture did not change the final expansion rate significantly. This resulted in an increase in the IOT admixture with more IOTs in the same volume of sample, which was the main reason for the increase in bulk density. In addition,

the variations between the compressive strength and bulk density are consistent with previous studies in that bulk density is positively correlated with compressive strength, with higher bulk density resulting in higher compressive strength. In this section, the reasons for the increase in the compressive strength are manifold. Pore structure and hydration products are two important factors. As the IOT admixture increases, more IOTs in the slurry fill the voids between the hydration products and refine the pore structure, which will be discussed in detail in Section 3.6. In addition, the Ca/Si ratio also influences the hydration products of AAC, with sand-based AAC and ash-based AAC having different Ca/Si ratio systems. The Ca/Si ratio of sand-based AAC is usually less than that of ash-based AAC. As the IOT content increases, more silica ions are introduced into the AAC production system, and the Ca/Si ratio tends to be optimal for sand-based AAC (<0.7). Lower Ca/Si ratios are more likely to produce low alkali hydration products, which can form tobermorite under hydrothermal conditions, making it easier for AAC products to achieve high strength. To further illustrate the quality of AAC, the standard specification (GB/T 11968-2020 [21]) is listed in Table 3, and in conjunction with Figure 6, all AAC samples met the standard.

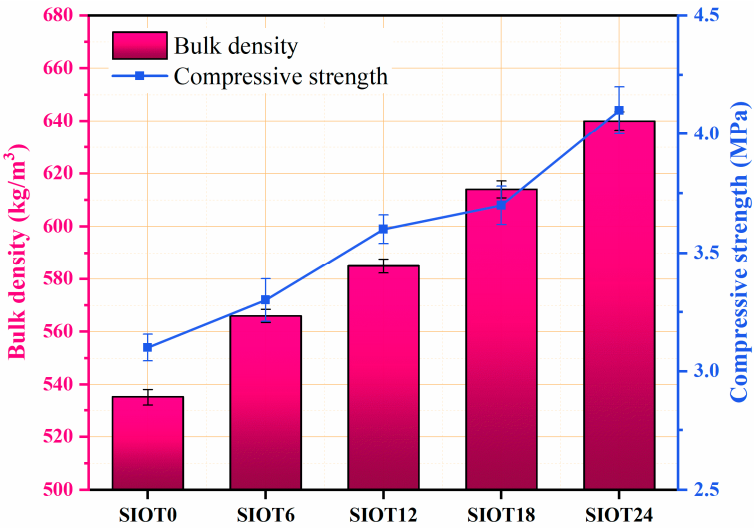

Figure 6. Compressive strengths and bulk densities of individual groups of samples.

Table 3. Standard specification for AAC (GB/T 11968-2020).

Strength Grade	Compressive Strength (MPa)		Bulk Density Grade	Average Bulk Density (kg/m^3)
	Max. Value	Min. Value		
A3.5	≥3.5	≥3.0	B05 B06	≤550 ≤650

3.5. Characterization of Reaction Products

3.5.1. XRD

The XRD patterns of the pre-autoclave and post-autoclave samples are shown in Figure 7a,b. In the XRD patterns of the pre-autoclave samples, there is no significant change in the mineral phase. The main mineral phases were quartz, calcite, and albite, accompanied by minor minerals C_2F, C_2S, and RO, which were inherited from the raw steel slag. It is noteworthy that the peak intensity of quartz increases with the increasing IOT content. As a result, IOTs with low activity are not or only marginally involved in hydration before autoclaving.

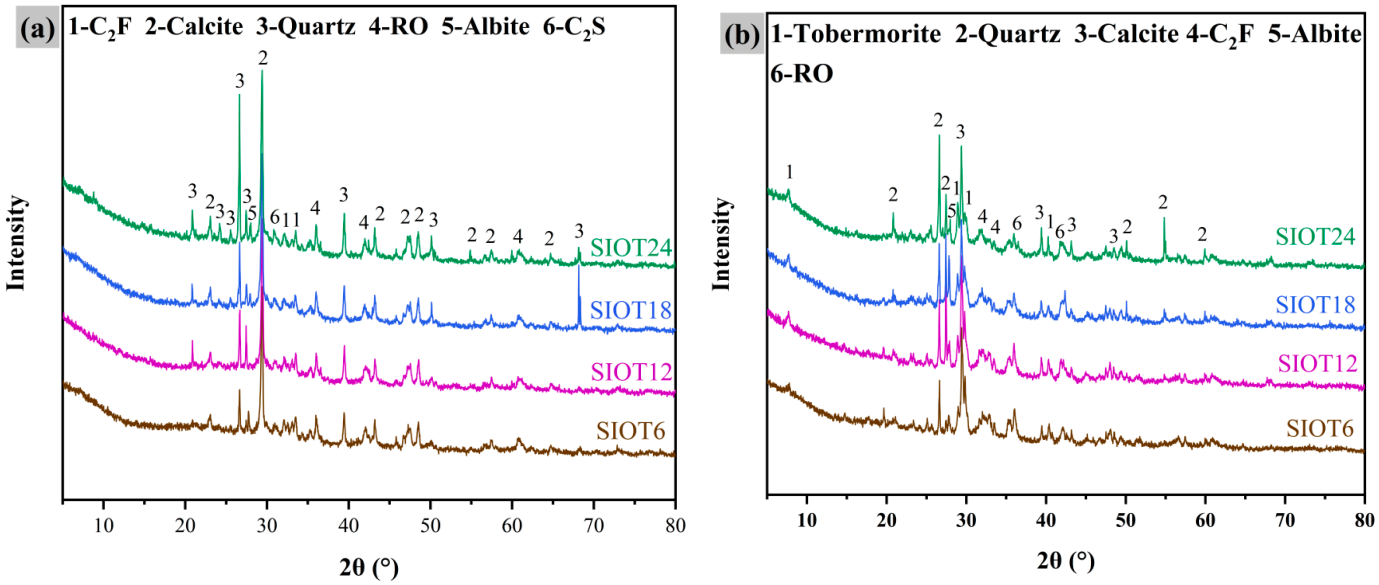

Figure 7. XRD patterns of AAC samples with different IOTs contents: (**a**) samples before autoclaving; (**b**) autoclaved samples.

As shown in Figure 7b, the key crystalline phases of tobermorite can be observed. In addition, the mineral phases quartz, C_2F, calcite, albite, and RO were also observed in the samples after autoclaving. It is worth noting the weakening and disappearance of the quartz diffraction peak and the disappearance of the C_2S diffraction peak. Meanwhile, tobermorite peaks are identified in the XRD pattern. In combination with Figure 7, the activities of quartz and C_3S in the feedstock increase under hydrothermal conditions; hence, the siliceous and calcareous feedstocks are further consumed to form tobermorite as the reactions progress. In addition, the elevated IOT content leads to more incompletely dissolved and reacted IOTs in the AAC product. The intensity of quartz in the autoclaved sample SIOT24 was significantly higher than in the other three samples, indicating that excess IOTs do not fully participate in the hydrothermal reaction but exist in the AAC products as an inactive filler. In this regard, while the excess IOTs introduced too much unreactive filler, they also facilitated the formation of tobermorite, which may have contributed to the change in AAC properties. Furthermore, inactive crystalline minerals such as albite, C_2F, and RO identified in the AAC before autoclaving are still present in the XRD pattern after autoclaving.

3.5.2. TG/DTG

The TG-DTA curves for the autoclaved samples are indicated in Figure 8. Below 85 °C, the losses of physically bound water in blocks result in minor DTG peaks at the beginning of the curves. At temperatures between 85 °C and 1000 °C, it is clear that all samples showed significant endothermal peaks of DTG curves at approximately 100 °C, 380 °C, 620 °C, and 830 °C, which are associated with the decomposition of hydrates such as CSH, tobermorite, and calcium carbonate. The mass losses are divided into four stages: 85–300 °C, 300–450 °C, 650–780 °C, and 780–850 °C. The mass loss range of 85–300 is attributed to the removal of bound water by the CSH gel. Furthermore, the mass loss at 300 to 450 °C in Figure 8 is associated with the dehydration of tobermorite. With further heating, very strong mass loss is found between 650–780 °C, which is related to the decomposition of carbonated phases. Finally, the peaks observed in the range of 780–850 °C are assigned to the crystal transformation of tobermorite. Above 850 °C, weak peaks may be associated with the formation of wollastonite [20].

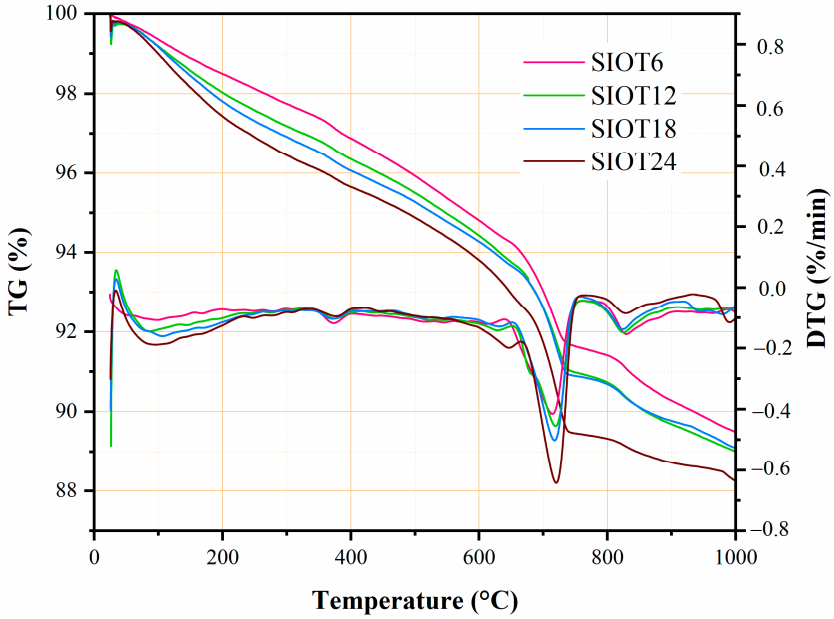

Figure 8. TG/DTG analysis of individual groups of samples.

3.5.3. FTIR

Figure 9 shows the FTIR spectra of the SIOT6-SIOT24 AAC samples within the wavenumber range of 4000–400 cm^{-1}. The broad bands detected at approximately 3480 cm^{-1} are assigned to the bending vibration of O-H in C-S-H or molecular water. Moreover, the vibration bands at approximately 1630 cm^{-1} are believed to be symmetric stretching of O-H. The different vibrational modes of carbonate can be observed in all samples, and the peaks include 875 cm^{-1} ($\nu_2[CO_3]^{2-}$), 1425 cm^{-1} ($\nu_3[CO_3]^{2-}$), 1452 cm^{-1} ($\nu_3[CO_3]^{2-}$), 1486 cm^{-1} ($\nu_3[CO_3]^{2-}$), and a combination band at 1798 cm^{-1} (2 $\nu_2[CO_3]^{2-}$) [22]. The relatively broad band range of 900–1100 cm^{-1} is thought to be relevant for the asymmetric stretching vibration of Si-O [23]. As the IOT content increased, it is clear that several sharp peaks gradually disappeared in the band area between 900 and 1100 cm^{-1}. The band near 900–1100 cm^{-1} then becomes wide and eventually turns into a broad range of absorption bands. This is thought in the literature to be caused by the antisymmetric stretching vibration of Si-O nonbridging oxygen [24]. Interestingly, the bending vibration of the Si-O-Si absorption peak appears in the band of the SIOT24 sample located at 676 cm^{-1}, which is the typical vibrational band of tobermorite. It has been demonstrated that the incorporation of Al causes a change in the absorption intensity and position of this band. This may be related to the formation of Al-substituted tobermorite [25]. The bands near 750 cm^{-1} and 710 cm^{-1} are related to the presence of albite, which is consistent with the XRD pattern results (Figure 7). The peaks centered at approximately 488 cm^{-1} are related to Si-O bonds. Additionally, the band in this area shifted to low wavenumbers, indicating the formation of silicates with higher polymerization degrees. Subsequently, the bands at approximately 439 cm^{-1} were ascribed to SiO_4 tetrahedral vibrations. The peaks appearing at 512 cm^{-1} correspond to the presence of quartz in the IOTs.

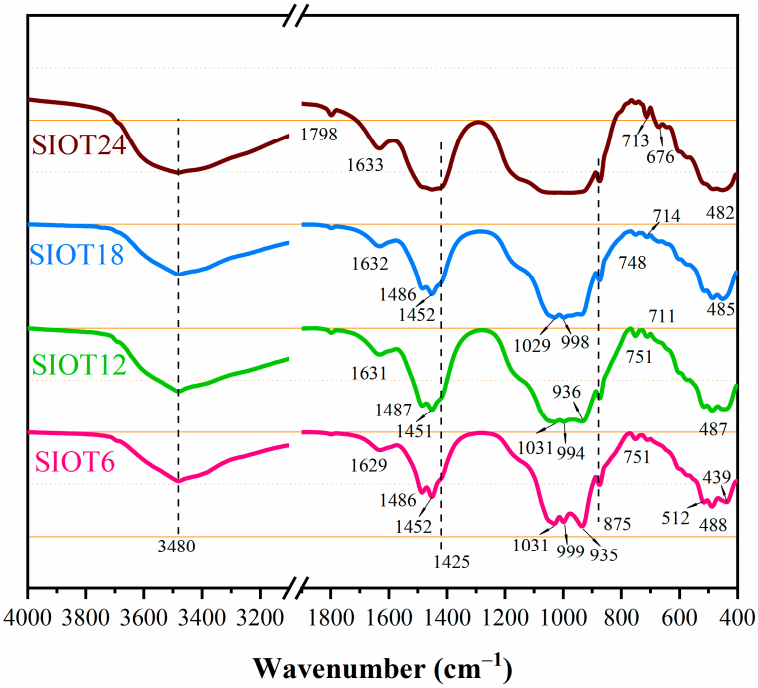

Figure 9. FTIR analysis of individual samples.

3.5.4. SEM/EDS

The microstructure of AAC samples with different IOT contents and the selected representative EDS points are displayed in Figure 10. Figure 10a,b shows the microscopic morphology of tobermorite on the hole walls of samples SIOT6 and SIOT24, respectively. It is obvious that the morphology of tobermorite on the pore wall changes significantly. The tobermorite of specimen SIOT24 becomes wider and thicker into thick flakes, while the tobermorite of SIOT6 appears as long strips. Compared with the elongated tobermorite, the slice-shaped tobermorite is more closely bound on the surface of the hole wall of the AAC, and this kind of tobermorite is considered to have a relatively high crystallinity. Figure 10(a1,b1) shows the EDS analysis of the two types of tobermorite. Slice-shaped tobermorite has a Ca/Si ratio of 0.843, close to 0.83 of the pure phase, while the Ca/Si ratio of long-strip-shaped tobermorite was 0.784, lower than that of the pure phase. In addition to tobermorite on the pore wall, the tobermorite in the interior of the sample with CSH and quartz particles, and not yet participating in the reaction of inert raw materials, formed a dense whole by interfingering and padding with each other. Figure 10c shows the microstructure of the SIOT24 section of the sample. It can be seen that the quartz particles interconnected with CSH and tobermorite. Beyond that, the growth of tobermorite on the quartz surface was observed, as illustrated in Figure 10d. Quartz is not only used as a physical filler aggregate but also as a carrier for the growth of tobermorite. The interlaced growth of tobermorite on its surface connects the surrounding hydration products, refining the pore structure and thus improving the compressive strength. In Figure 10(c1), the EDS image results indicated that the Ca/Si ratio of the long-strip-shaped tobermorite was 0.776.

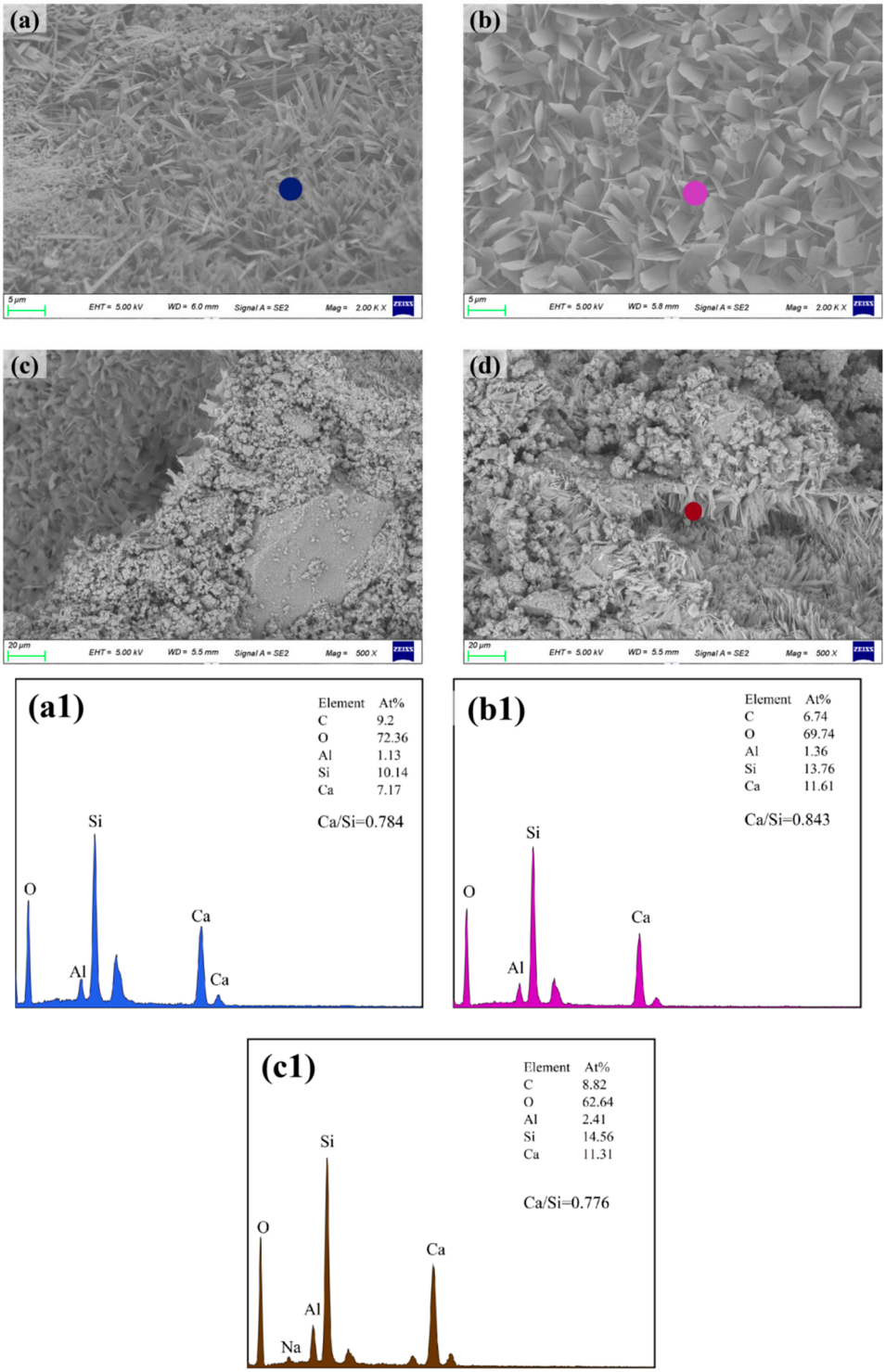

Figure 10. SEM analysis of samples and EDS points: (**a**,**a1**) SIOT6; (**b**–**d**,**b1**,**c1**) SIOT24.

3.6. MIP

AAC is a porous material in which the pores vary in size and distribution. Mercury intrusion porosimetry (MIP) is widely used as a comparative measurement tool for porous systems of concrete materials.

The porosities of the AAC samples determined by MIP are illustrated in Table 4. As shown in Table 4, samples SIOT6, SIOT12, SIOT18, and SIOT24 display porosities of 64.25%, 59.75%, 56.76%, and 54.21%, respectively. The higher the content of IOTs is, the lower the

porosity. This is because the high content of IOTs reduces the fluidity of the slurry and therefore limits the foaming process.

Table 4. Porosities of individual samples.

Samples	SIOT6	SIOT12	SIOT18	SIOT24
Porosity	64.25%	59.75%	56.76%	54.21%

The cumulative pore volume and incremental pore volume of samples SIOT6-SIOT24 are presented in Figures 11 and 12. First, the cumulative intrusion that shows a high value with high IOT content from the pore size range of 0.01–0.1 µm suggests the formation of a dense pore structure. Second, as shown in Figure 11, it can be clearly seen that the pore size between 0.01–5 µm is shifted to the left, indicating that the pore structure of AAC is refined as the IOT content increases. The slurry fluidity is critical in the development of the AAC pore structure distribution, which will be discussed in detail in Section 3.7.1. In addition, the IOTs act as a carrier for the growth of tobermorite, which intersperses with the surrounding tobermorite to fill the pores and adjust the pore structure. Again, the quantity of the pore size range of 60–130 µm increases with the increasing IOTs. In summary, high IOT content refined the pore structure, yielding more small-sized pores, and the number of large pores increased slightly.

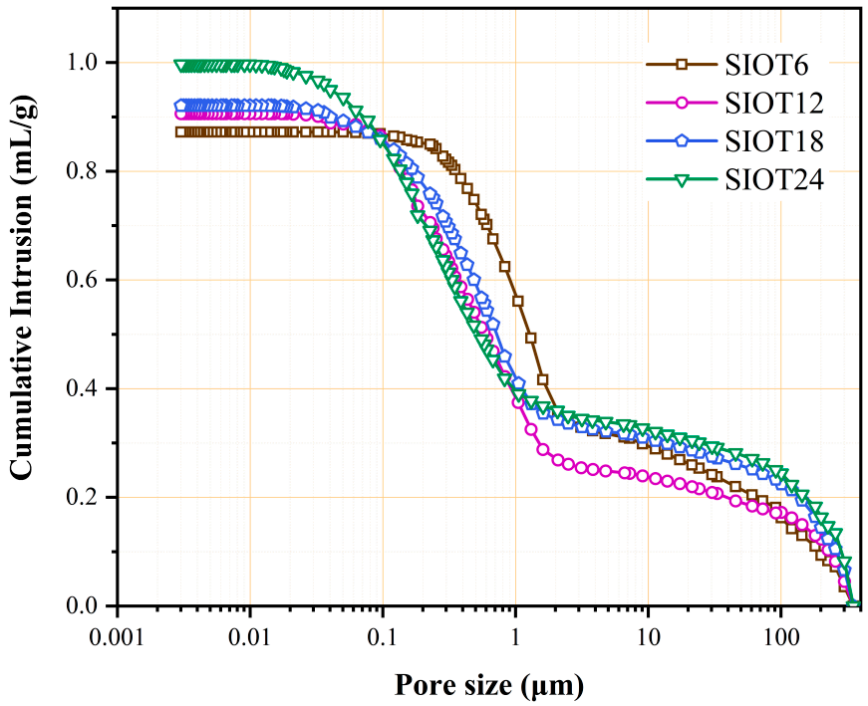

Figure 11. Results of the MIP experiment: cumulative pore volumes of individual samples.

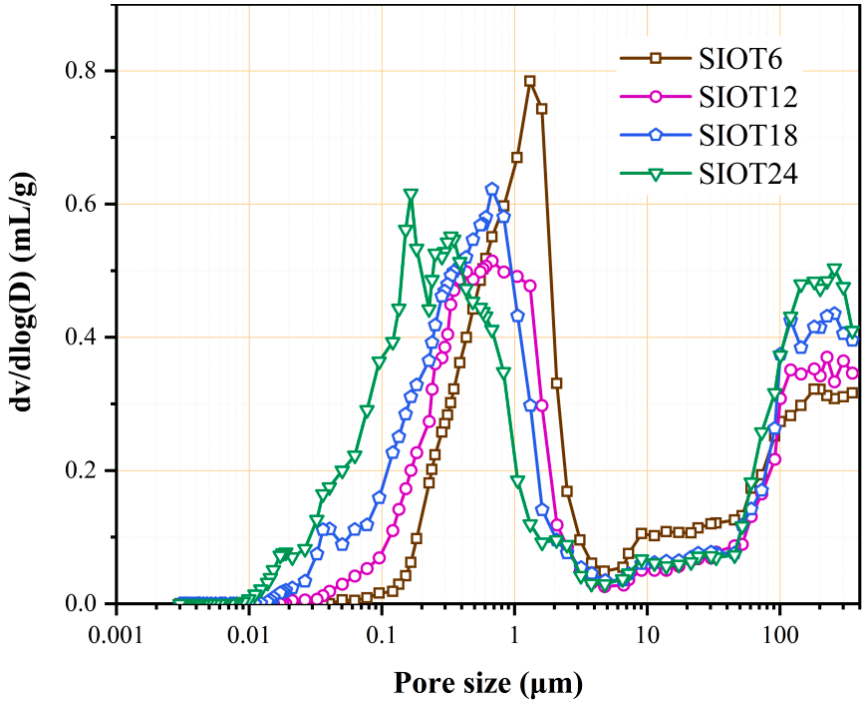

Figure 12. Results of the MIP experiment: incremental pore volumes of individual samples.

3.7. General Discussion

3.7.1. The Fluidity of the Slurry and Pore Size Distribution

The pore size distribution plays an important role in the quality of the final AAC products. However, the refinement of the pore structure promotes the development of compressive strength. However, the formation of numerous small pores resulting in the block yields a high bulk density. High bulk density prevents AAC products from meeting application requirements. Moreover, a large number of macropores can lead to a stress concentration for the AAC product, which reduces the compressive strength. Hence, it is necessary to analyze the pore size distribution of AAC. Slurry fluidity is an important parameter affecting the distribution and number of pores in the AAC product. The correlations between the slurry fluidity and pore size distribution are plotted in Figure 13. The pores in the AAC samples were divided into three groups: gel pores (<0.05 μm), capillary pores (0.05–60 μm), and macropores (>60 μm) [26,27]. Considering the specific pore size distribution in the AAC samples, the capillary pores were further divided into three groups: 0.05–0.5 μm, 0.5–10 μm, and 10–60 μm. Clearly, the numbers of gel pores, macropores, and pores in the range of 0.05–0.5 μm increase significantly with the increasing slurry fluidity. In addition, the percentage of pores in the 10–60 μm pore size range is small and decreases slightly with increasing fluidity.

In summary, slurries with higher fluidity present a denser pore structure. The slurry with high fluidity more easily fills the distances between the hydration products and raw material particles during the foaming process. In addition, the IOTs are not only used as the filling aggregate but also as the carrier for the growth of tobermorite. They are connected with the surrounding hydrated product crystals to form a dense network structure, which also optimizes the pore structure.

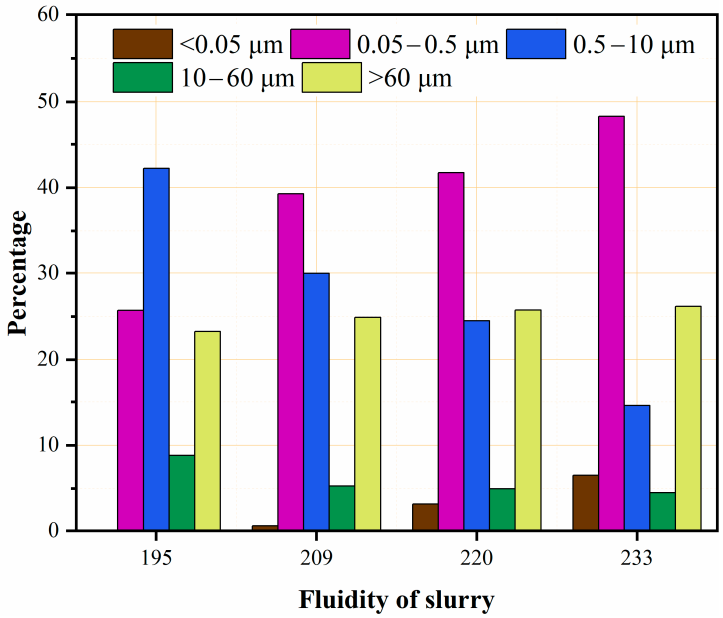

Figure 13. Influence of slurry fluidity on pore size distribution.

3.7.2. Strength Formation Mechanism of Sand-Based AAC

In contrast to ash-based AAC, sand-based AAC utilizes mainly low-activity siliceous raw materials. Highly reactive siliceous materials react quickly with lime to form C-S-H gels, which are subsequently converted to tobermorite (Equations (1) and (2)), whereas most low-activity materials are converted directly to tobermorite (Equation (3)). In the AAC products mixed with IOTs, a large amount of IOTs remains uninvolved in the reaction, while the raw material conversion rate of IOT AAC is high. However, the performance of sand-based AAC is generally better than that of ash-based AAC due to its similar structure to that of normal concrete. As shown in Figure 14, as the autoclaved reaction progresses, the IOTs are gradually activated with the release of Si^{4+}, and the external quartz sand gradually reacts with the calcareous materials in the slurry to form tobermorite, while the unreacted IOTs are present in the AAC product in an aggregate-like form. The less reactive siliceous raw materials in sand AAC participate in the reaction and bind more tightly to the surrounding tobermorite than in normal concrete, and the unreacted IOTs therefore combine with the tobermorite to form a monolith that is stronger than the pure tobermorite phase.

$$Ca^{2+} + Si^{4+} \xrightarrow{\text{Hydration}} CSH + Ca(OH)_2 + Si^{4+} \rightarrow CSH \quad (1)$$

$$CSH \xrightarrow{\text{Hydrothermalsynthesis}} \alpha - C2SH + Si^{4+} \xrightarrow{\text{Hydrothermalsynthesis}} C5S6H5 \quad (2)$$

$$IOT \xrightarrow{\text{Hydrothermalsynthesis}} Ca^{2+} + Si^{4+} + Ca(OH)_2 \xrightarrow{\text{Hydrothermalsynthesis}} C5S6H5 \quad (3)$$

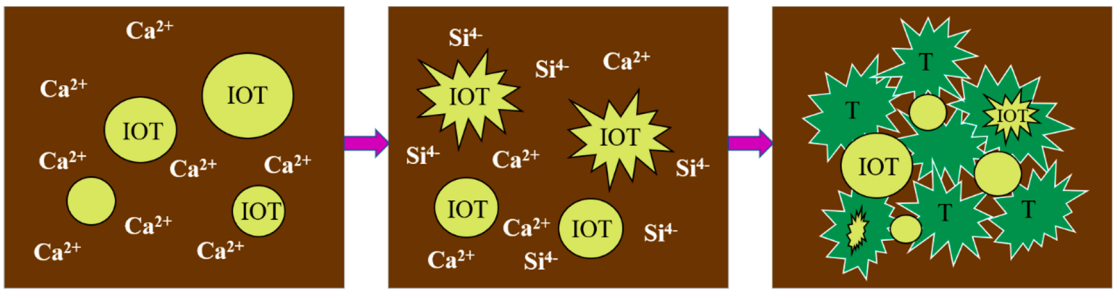

Figure 14. Structural transformation of sand-based AAC (IOTs = IOTs, T = tobermorite).

4. Conclusions

In this paper, the following conclusions were drawn by studying the effects of different IOT admixtures in steel slag-based AAC.

1. With the increase in the IOT admixture, the pH of the slurry decreased from 12.65 to 12.47, the fluidity increased from 191 mm to 233 mm, the final expansion rate of the slurry was approximately 92%, and the end time of gas generation was 69–90 min.
2. The compressive strength and bulk density of the AAC increased with the increasing IOT admixture, and the compressive strength of the samples increased from 3.1 MPa to 4.1 MPa; meanwhile, the bulk density increased from 535 kg/m^3 to 640 kg/m^3, and all the AAC samples met the requirements of the standard specification (GB/T 11968-2020) grade A3.5.
3. With the increase in the IOT admixture, the tobermorite became wider and thicker, and the quartz particles interlinked with CSH and tobermorite to form a dense whole.
4. The high IOT admixtures refined the pore structure and produced more small-sized pores, with the number of pores less than 0.05 μm increasing by 6% and the number of pores in the 0.05–0.5 μm range increasing by 23%.
5. In sand-based AAC, the IOTs not only act as a filler material but also as a carrier for the growth of tobermorite, which intersects with the surrounding tobermorite to form a whole structure with the IOTs as the skeleton, and the overall strength is high compared to that of pure tobermorite.

Author Contributions: Methodology, J.W.; Software, H.Z. (Houhu Zhang); Validation, J.W.; Formal analysis, B.Q.; Investigation, H.Z. (Hao Zhou); Resources, Y.J.; Data curation, B.Q.; Writing—original draft, H.Z. (Hao Zhou); Writing—review & editing, B.M.; Visualization, B.M.; Supervision, Y.H.; Project administration, Y.J. and H.Z. (Houhu Zhang); Funding acquisition, Y.H. All authors have read and agreed to the published version of the manuscript.

Funding: This work was supported by the Primary Research and Development Plan of Jiangsu Province (Grant No. BE2021684), the Natural Science Foundation of Jiangsu Province of China (Grant No. BK20220701), and the Basic Business of the Central Public Welfare Research Institute of China (Grant Nos. GYZX180102 and GYZX170304), financial support of the Special Fund of the Chinese Central Government for Basic Scientific Research Operations in the Commonweal Research Institute (Grant No. GYZX220301) and the Special Fund of the Carbon Peak and Carbon Neutrality Research Institute supported by Nanjing Institute of Environmental Sciences, Ministry of Ecology and Environment (Grant No. ZX2023SZY060).

Data Availability Statement: The data that used in this study can be required from the corresponding author. The data are not publicly available due to information that could compromise reseach participant privacy.

Conflicts of Interest: The authors declare no conflict of interest.

References

1. Mesecke, K.; Malorny, W.; Warr, L.N. Understanding the effect of sulfate ions on the hydrothermal curing of autoclaved aerated concrete. *Cem. Concr. Res.* **2023**, *164*, 107044. [CrossRef]
2. Narayanan, N.; Ramamurthy, K. Structure and properties of aerated concrete: A review. *Cem. Concr. Compos.* **2000**, *22*, 321–329. [CrossRef]
3. Jiang, J.; Cai, Q.; Ma, B.; Hu, Y.; Qian, B.; Ma, F.; Shao, Z.; Xu, Z.; Wang, L. Effect of ZSM-5 waste dosage on the properties of autoclaved aerated concrete. *Constr. Build. Mater.* **2021**, *278*, 122114. [CrossRef]
4. Pacheco-Torgal, F.; Labrincha, J.A.; Leonelli, C.; Palomo, A.; Chindaprasirt, P. *Handbook of Alkali-Activated Cements, Mortars and Concretes*; Woodhead Publishing: Thorston, UK, 2015.
5. Xue, W.; Xu, L.; Wang, Z.; Min, T.; Xu, J. Experimental study on seepage evolution and microscopic characteristics of initially damaged concrete under variable confining pressure. *Constr. Build. Mater.* **2023**, *393*, 132157. [CrossRef]
6. Li, C.; Sun, H.; Bai, J.; Li, L. Innovative methodology for comprehensive utilization of iron ore tailings: Part 1 The recovery of iron from iron ore tailings using magnetic separation after magnetizing roasting. *J. Hazard. Mater.* **2010**, *174*, 71–77. [CrossRef]
7. Zhao, J.; Ni, K.; Su, Y.; Shi, Y. An evaluation of iron ore tailings characteristics and iron ore tailings concrete properties. *Constr. Build. Mater.* **2021**, *286*, 122968. [CrossRef]

8. Cai, L.; Li, X.; Liu, W.; Ma, B.; Lv, Y. The slurry and physical-mechanical performance of autoclaved aerated concrete with high content solid wastes: Effect of grinding process. *Constr. Build. Mater.* **2019**, *218*, 28–39. [CrossRef]
9. Xue, W.; Twenda, C.; Alam, M.S.; Xu, L.; Wang, Z. Experimental study on seepage characteristics and stress sensitivity of desulfurization gypsum based concrete under triaxial stress. *J. Mater. Res. Technol.* **2023**, *24*, 6425–6437. [CrossRef]
10. Xue, W.; Wang, Z.; Alam, M.S.; Xu, L.; Xu, J. Mechanical and seepage characteristics of polyvinyl alcohol fiber concrete under stress-seepage coupling. *J. Build. Eng.* **2023**, *78*, 107694. [CrossRef]
11. Bhatia, S.; Beltramini, J.; Do, D.D. Deactivation of zeolite catalysts. *Catal. Rev.* **1989**, *31*, 431–480. [CrossRef]
12. Petushkov, A.; Yoon, S.; Larsen, S.C. Synthesis of hierarchical nanocrystalline ZSM-5 with controlled particle size and mesoporosity. *Microporous Mesoporous Mater.* **2011**, *137*, 92–100. [CrossRef]
13. Zhou, L.; Wang, A.; Li, H.; Zhou, W.; Wang, J.; Luo, Y.; Qian, B.; Liang, R.; Gao, H.; Li, Y.; et al. Effects of curing temperature and water glass modulus on the preparation of hierarchical zeolite precursors. *Silicon* **2023**, *15*, 4585–4601. [CrossRef]
14. Jiang, J.; Ma, B.; Cai, Q.; Shao, Z.; Hu, Y.; Qian, B.; Wang, J.; Ma, F.; Wang, L. Utilization of ZSM-5 waste for the preparation of autoclaved aerated concrete (AAC): Mechanical properties and reaction products. *Constr. Build. Mater.* **2021**, *297*, 123821. [CrossRef]
15. Xue, W.; Jing, W.; Wang, Z.; Zhang, H.; Lin, J. Mechanical behavior and constitutive model of lining concrete in triaxial compression infiltration process under pore water pressure. *Arch. Civ. Mech. Eng.* **2023**, *23*, 20. [CrossRef]
16. *GB/T 2419–2005*; Test Method for Fluifity of Cement Mortar. Standards Press of China: Beijing, China, 2015.
17. *GB/T 11969–2008*; Test Methods of Autoclaved Aerated Concrete. Standards Press of China: Beijing, China, 2008.
18. Cao, L.; Zhou, J.; Zhou, T.; Dong, Z.; Tian, Z. Utilization of iron tailings as aggregates in paving asphalt mixture: A sustainable and eco-friendly solution for mining waste. *J. Clean. Prod.* **2022**, *375*, 134126. [CrossRef]
19. Cong, X.Y.; Lu, S.; Yao, Y.; Wang, Z. Fabrication and characterization of self-ignition coal gangue autoclaved aerated concrete. *Mater. Des.* **2016**, *97*, 155–162. [CrossRef]
20. Xue, W.; Min, T.; Alam, M.S.; Fan, H.; Liu, L. Evolution characteristics and mechanism of concrete performance under water pressure environment: A comprehensive review. *Struct. Concr.* **2023**, *24*, 6338–6369. [CrossRef]
21. *GB/T 11968–2020*; Autoclaved Aerated Concrete Blocks. Standards Press of China: Beijing, China, 2020.
22. Reig, F.B.; Adelantado, J.V.G.; Moreno, M.C.M.M.J.T. FTIR quantitative analysis of calcium carbonate (calcite) and silica (quartz) mixtures using the constant ratio method. *Appl. Geol. Samples* **2002**, *58*, 811–821.
23. Mostafa, N.Y.; Kishar, E.A.; Abo-El-Enein, S.A. FTIR study and cation exchange capacity of Fe^{3+} and Mg^{2+} substituted calcium silicate hydrates. *J. Alloys Compd.* **2009**, *473*, 538–542. [CrossRef]
24. Yang, F.; Zhu, Y.; Li, J.; Wang, C.; Ren, Z.; Cui, X. Preparation and performance of energy-saving and environment-friendly autoclaved. *J. New Mater. Electrochem. Syst.* **2019**, *22*, 149–154. [CrossRef]
25. Guo, X.; Meng, F.; Shi, H. Microstructure and characterization of hydrothermal synthesis of Al-substituted tobermorite. *Constr. Build. Mater.* **2017**, *133*, 253–260. [CrossRef]
26. Alexanderson, J. Relations between structure and mechanical properties of autoclaved aerated concrete. *Cem. Concr. Res.* **1979**, *9*, 507–514. [CrossRef]
27. Petrov, I.; Schlegel, E. Application of automatic image analysis for the investigation of autoclaved aerated concrete structure. *Cem. Concr. Res.* **1994**, *24*, 830–840. [CrossRef]